ChemPubSoc Europe

DOI: 10.1002/cphc.201800723

CHEMPHYSCHEM Articles

Origin of Nb_2O_5 Lewis Acid Catalysis for Activation of Carboxylic Acids in the Presence of a Hard Base

Pussana Hirunsit,*[a] Takashi Toyao,[b, c] S. M. A. Hakim Siddiki,[b] Kenichi Shimizu,*[b, c] and Masahiro Ehara*[c, d]

The Nb_2O_5 surface catalyzes the amidation of carboxylic acids with amines through Nb^{5+} Lewis acid activation of the C=O group. In this work, DFT calculations were applied to theoretically investigate the C=O bond activation of a model carboxylic acid (acetic acid) on θ-Al_2O_3(110), anatase TiO_2(101), and T-Nb_2O_5 (100) surfaces. The adsorption sites, adsorption energies, reaction energy barriers, electronic properties, and vibrational frequency of acetic acid were examined in detail. It was found that the bond activation of the carbonyl group is most efficient on Nb_2O_5, although the adsorption energy is larger on Al_2O_3 and TiO_2. The most efficient C=O bond activation on Nb_2O_5 results in the lowest energy barrier of C–N bond formation during amidation. The Nb_2O_5 surface also shows larger tolerance to methylamine and water molecules than Al_2O_3 and TiO_2 surfaces. These crucial factors contribute to the highest amidation catalytic reactivity on Nb_2O_5. Furthermore, the position of the mean density of states of the *d*-conduction band of the active metal site relative to the Fermi energy level correlates well with the efficiency in the C=O bond activation and, consequently, the catalytic activity for amidation. These results suggest that, unlike a classical understanding of strong acid sites of metal oxide surfaces, interaction of a carbonyl HOMO with an unoccupied metal *d*-orbital, or, in other words, covalent-like interaction between a carbonyl group and metal adsorption site, is relevant to the present system.

1. Introduction

Lewis acids can promote nucleophilic substitution reactions of carbonyl compounds, but not when the nucleophiles have strong basicity. In principle, Lewis acids are deactivated by strong coordination of basic substrates (such as amines). In condensation reactions, water (coproduct) has a greater affinity for Lewis acids than carboxylic acids and deactivates the Lewis acids. Amide synthesis from carboxylic acids (and their derivatives) and amines is a typical example of nucleophilic substitution reactions of carbonyl compounds with a strong base. Hence, amide condensation by Lewis acid catalysts remains a challenging reaction. Conventionally, amides and imides are synthesized from (di)carboxylic acids and amines via activated carboxylic acid derivatives, such as carboxylic acid anhydrides or acyl chlorides, or using stoichiometric amounts of condensation reagents,[1] which generates large amounts of unwanted coproducts.

Recently reported methods for the amidation of carboxylic acids or its derivatives with amines, using homogeneous Lewis acid catalysts, are of importance due to their high atom efficiency.[2] However, these methods suffer from low catalytic efficiency, and difficulties associated with catalyst reuse and catalyst/product separation. To develop a practical Lewis acid catalyst for amidation reactions, one should design a heterogeneous Lewis acid catalyst that preferentially interacts with the carbonyl group of a carboxylic acid in the presence of a strong base (amine and water), as proposed in a recent study.[3]

Recently, one of the authors of this paper (Shimizu), together with other coworkers, reported a new heterogeneous Lewis acid catalyst, Nb_2O_5, which exhibits high catalytic performance and good catalyst reusability for four types of amidation reactions: synthesis of amides from amines with carboxylic acids (reaction 1) or esters (reaction 2) and synthesis of cyclic imides from amines with dicarboxylic acids (reaction 3) or dicarboxylic anhydrides (reaction 4) (see Figure 1).[4–7] The selected results of catalyst screening tests for these reactions are also shown in Figure 1. Interestingly, the catalytic activity of the metal oxides in all the reactions changes in the following order: $Nb_2O_5 > TiO_2 > \theta$-Al_2O_3. It should be noted that Nb_2O_5 shows the best performance among these catalysts even if the activities are normalized by their BET specific surface areas (54 $m^2 g^{-1}$ for Nb_2O_5, 45 $m^2 g^{-1}$ for TiO_2, and 74 $m^2 g^{-1}$ for θ-

[a] Dr. P. Hirunsit
National Nanotechnology Center
National Science and Technology Development Agency
111 Thailand Science Park, Pathum Thani 12120, Thailand
E-mail: pussana@nanotec.or.th
[b] Dr. T. Toyao, Dr. S. M. A. H. Siddiki, Prof. Dr. K. Shimizu
Institute for Catalysis, Hokkaido University
Kita 21 Nishi 10, Kita-ku, Sapporo, Hokkaido 001-0021, Japan
E-mail: kshimizu@cat.hokudai.ac.jp
[c] Dr. T. Toyao, Prof. Dr. K. Shimizu, Prof. Dr. M. Ehara
Elements Strategy Initiative for Catalysts and Batteries (ESICB)
Kyoto University, Kyoto 615-8520, Japan
E-mail: ehara@ims.ac.jp
[d] Prof. Dr. M. Ehara
Institute for Molecular Science
Nishigo-naka 38, Myodai-ji, Okazaki, Aichi 444-8585, Japan

Supporting information for this article is available on the WWW under https://doi.org/10.1002/cphc.201800723

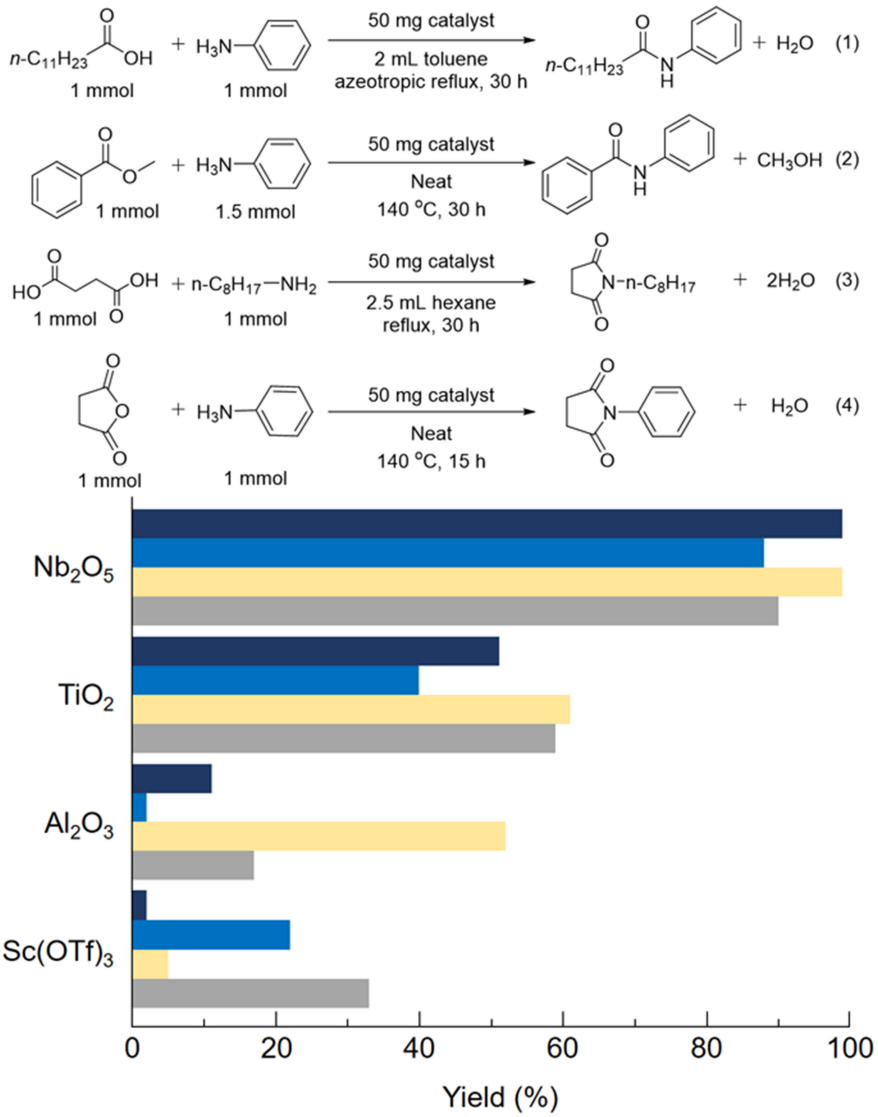

Figure 1. Catalytic results for amidation-type reactions (1–4): (1) amide yield from carboxylic acid and amine (navy bar),[4] (2) amide yield from ester and amine (blue bar),[5] (3) cyclic imide yield from dicarboxylic acid and amine (yellow bar),[6] and (4) cyclic imide yield from dicarboxylic anhydride and amine (gray bar).[7]

Al_2O_3). The activity of Nb_2O_5 is even higher than that of $Sc(OTf)_3$, a well-known homogeneous water-tolerant Lewis acid catalyst.[8,9]

To explain the reasons for the activity order, they carried out kinetic and infrared (IR) experiments. IR results of pyridine adsorption on these metal oxides showed a predominantly Lewis acidic nature of these catalysts. IR spectra of a model carboxylic acid (acetic acid) at −75 °C showed that the C=O stretching band of the adsorbed acetic acid ($\nu_{C=O}$) on Nb_2O_5 was located at lower wavenumber (1686 cm^{-1}) than that those of Al_2O_3 (1697 cm^{-1}) and TiO_2 (1695 cm^{-1}).[4] Results indicate that the interaction between the Lewis acid site (Nb^{5+} cation) on the surface of Nb_2O_5 and the carbonyl group results in weaker carbonyl C=O bond than the sites of other Lewis acidic oxides (Al_2O_3 and TiO_2). The acid–base interaction between the Nb^{5+} Lewis acid site and carbonyl group can increase the electrophilicity of the carbonyl group, which results in high reactivity of the carboxyl acid (or ester) with a nucleophile, amine. Kinetic studies suggest that Lewis acid sites of Nb_2O_5 are less negatively affected by basic molecules (amines, water) in solution than other Lewis acidic oxides (Al_2O_3 and TiO_2) and homogeneous Lewis acid catalysts.[4] Experimental evidence suggests that the high activity of Nb_2O_5 for amidation-type reactions is due to its base-tolerant Lewis acidity, as well as suitable acid–base interaction between the Nb^{5+} Lewis acid site and carbonyl oxygen, which increases the reactivity of the carbonyl group with amines. To verify this hypothesis, a theoretical study is required to achieve an atomic level understanding of the selective activation mechanism.

In this study, we apply density functional theory (DFT) calculations to examine the adsorption of CH_3COOH, CH_3NH_2, and H_2O and the energy barrier for amidation on θ-Al_2O_3, TiO_2, and Nb_2O_5 surfaces. The catalytic activity trend among these metal oxides can be described by the energy barrier, adsorption energy, the density of states (DOS) of catalytic active sites, the adsorbed geometric bond lengths, molecular vibrational fre-

quency, and the electronic charges. These properties enable us to describe the origin of the carbonyl C=O bond activation, the nature of the interaction between catalyst and the carbonyl oxygen atom, and base- and water-tolerance properties, leading to an understanding of the relatively high catalytic activity of the Nb_2O_5 catalyst.

2. Models and Computational Details

2.1. Bulk Structure

The phase of θ-Al_2O_3, anatase TiO_2 and T-phase of Nb_2O_5 were chosen because they were applied in the experiment.[4,5] The bulk structure of θ-Al_2O_3 has a monoclinic structure (Figure S1 in the Supporting Information). A unit cell consists of a total of twenty atoms, with eight Al atoms and twelve O atoms, having four formula units per unit cell. A 6×6×4 Monkhorst–Pack k-point mesh was applied. The calculated cell parameters and those obtained from the experiment[12] are shown in Table S1. The calculated parameters are in excellent agreement with what has been reported previously[13] and the experimental values; deviation is in the order of ~1%. These parameters are also sufficient for the total energy to converge within 0.001 eV.

The bulk structure of the T-phase of Nb_2O_5 is based on the reported structure.[14] The calculations employed 8×8×3 k-points Monkhorst–Pack mesh sampling in the surface Brillouin zone for the TiO_2 structure and 6×3×6 k-points mesh sampling for the T-Nb_2O_5 structure. The calculated lattice parameters of anatase TiO_2 and T-Nb_2O_5 are in excellent agreement with the experimental values.[14,17] They are reported in Table S1.

2.2. Surface Structure

The θ-Al_2O_3(110) surface is represented by a slab model with similar geometric details as applied in our previous work.[18] The (110) surface of the face-centered cubic (fcc) oxygen sublattice corresponds to (010) of the surface index of a monoclinic unit cell structure of θ-Al_2O_3.[19] Previous studies showed that the preferential exposed surface of θ-Al_2O_3 is the (110) surface of the fcc oxygen sublattice.[20,21] We employed the 2×1 supercell with a three θ-Al_2O_3 cell thickness slab containing 180 atoms and a vacuum region of ~15 Å in the z direction. It was previously found that the θ-Al_2O_3 charge-neutral slab was achieved with a three to four θ-Al_2O_3 cell thickness.[19] The θ-Al_2O_3(110) surface is shown in Figure 2(a). The θ-Al_2O_3(110) surface calculations employed a 2×2×1 k-points Monkhorst–Pack mesh sampling. All of the Al and O atoms, and adsorbate molecules, were fully optimized, except for the Al and O atoms on the bottom atomic layer of Al_2O_3, which were fixed to the calculated bulk distances.

The 3×1 supercell of the TiO_2(101) surface consisting of six Ti atomic layers and twelve oxygen atomic layers containing a total of 108 atoms and a vacuum region of ~15 Å in the z direction was applied. The TiO_2(101) surface structure is shown in Figure 2(b). The calculations employed 2×2×1 k-points

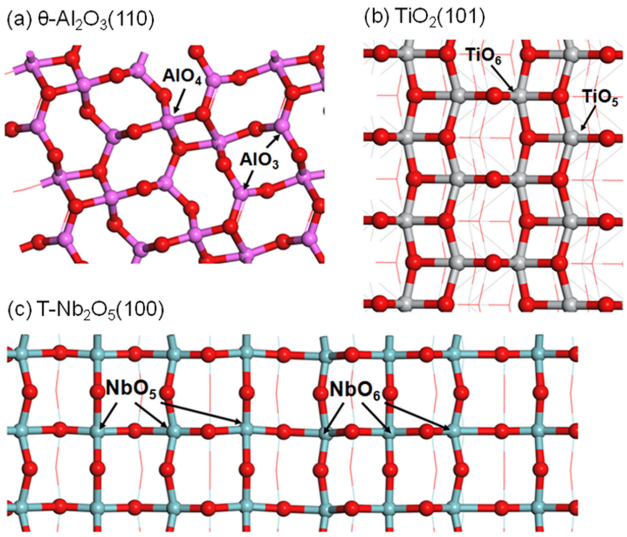

Figure 2. Top view of the clean surface structures and the possible active sites of (a) θ-Al_2O_3(110), (b) TiO_2(101), and (c) T-Nb_2O_5(100). AlO_3 and AlO_4 refer to an Al surface atom having atomic coordination numbers 3 and 4, respectively. TiO_5 and TiO_6 refer to a Ti surface atom having atomic coordination numbers 5 and 6, respectively. NbO_5 and NbO_6 refer to a Nb surface atom having atomic coordination numbers 5 and 6, respectively.

Monkhorst–Pack mesh sampling. The bottom two atomic layers of Ti atoms and four atomic layers of O atoms were fixed at their bulk optimized positions, while the rest were fully relaxed.

The T-Nb_2O_5(100) surface model was constructed from the calculated T-Nb_2O_5 bulk structure. The Nb terminated (100) surface was applied in this work because it was found to have the lowest surface energy.[22] The 1×2 supercell of T-Nb_2O_5(100) surface is applied in this work and contains a total of 168 atoms (48 Nb and 120 O atoms). The top view of T-Nb_2O_5(100) surface structure is shown in Figure 2c. The Nb surface atoms consist of 5 and 6 atomic coordination numbers (Figure 2c). The side view of T-Nb_2O_5(100) surface structure is shown in the Figure S2. The slab thickness of approximately 8.5 Å was employed and a vacuum region of ~15 Å was added in the z direction. Adsorbates and all atomic layers from the surface down to ~3 Å in the z direction were fully relaxed and the rest in the slab were fixed at their bulk positions. The reciprocal space was only sampled at the Γ k-point of the Brillouin zone due to the relatively large size of the slab unit cell. The similar T-Nb_2O_5 (100) surface model was previously applied for glycerol dehydration investigation.[22] It should be noted that deactivation of Nb_2O_5 catalyst was not experimentally found at least for several recycling tests.[4–7] The X-ray diffraction (XRD) measurements of Nb_2O_5 catalyst structure both before and after the amidation-type reactions is shown in Figure S3. The XRD patterns remained essentially the same after the reactions, indicating that the Nb_2O_5 catalyst is stable during the reactions.

2.3. General Computational Settings

The specific calculations parameters for each bulk and surface structures are described above and the general settings are

described in this section. The fully periodic plane-wave DFT calculations as implemented in the Vienna ab initio simulation program (VASP)[23,24] were employed. Spin-polarized DFT calculations were performed using the Perdew–Burke–Ernzerhof (PBE) exchange–correlation functional[10,11] described within the generalized gradient approximation (GGA) implemented with the projector augmented-wave function (PAW)[15,16] method for representing the nonvalence core electrons. The pseudopotentials were used to model the semi-core *p* states of Ti and Nb. The plane-wave cutoff energy was optimized at 400 eV. For the inclusion of long-range dispersion, the semiempirical dispersion potential correction method described by Grimme and coworkers[25,26] was applied. Gaussian broadening[27] was employed with a smearing width of 0.1 eV. The dipole corrections in all three spatial directions were included for isolated molecules calculations and only in z direction was included for surface calculations. The results were checked for convergence with respect to numbers of k-point and energy cutoff. The convergence criteria for electronic self-consistent iteration was set to 1.5×10^{-7} eV, and the ionic relaxation loop was limited for all forces smaller than 0.03 eV/Å for free atoms. Bader charge analysis was performed using VASP-VTST.[28–30] The transition state structures were located using nudged elastic band (NEB)[31] and dimer[32] methods. The transition state structures were characterized by a normal mode analysis to ensure that it has one imaginary frequency.

3. Results and Discussion

3.1. Carboxylic Acid, Methylamine, and Water adsorption

3.1.1. CH_3COOH Adsorption

The adsorption energy can be used as a preliminary probe of Lewis acidity of metal oxide surfaces. The adsorption energy (E_{ad}) was calculated by [Eq. (1)]:

$$E_{ad} = E_{total} - E_{clean\ surface} - E_{adsobate(isolated)} \quad (1)$$

where E_{total} is the energy of the system upon adsorption, $E_{cleansurface}$ is the energy of the clean surface, and $E_{adsobate(isolated)}$ is the energy of isolated adsorbate in gas phase. The calculated adsorption energies of the reactants on three metal oxide surfaces at the most stable structure in each site are summarized in Table 1. The adsorption energies of CH_3COOH on TiO_2(101) surface are in good agreement with those previously reported as shown in Table S2.

The amidation reaction on metal oxide surfaces commences with the Lewis acid activation of CH_3COOH, followed by nucleophilic amine attack on the carbonyl carbon of the adsorbed CH_3COOH. Thus, the C=O bond activation of CH_3COOH is a key factor in the reaction. Therefore, we now discuss the CH_3COOH adsorption. The adsorption of CH_3NH_2 and H_2O is discussed later in sections 3.1.2 and 3.1.3. The surface reactivity varies at different surface sites. This variation can be ascribed to the different coordination environments of the surface atoms. The adsorption energies for CH_3COOH were calculated at all metal cation sites with different coordination numbers. Different configurations are found on the three surfaces, where the OH group in CH_3COOH is dissociated or nondissociated. The dissociative adsorption of CH_3COOH shows that a proton adsorbs on the oxygen site of the surface and the CH_3COO^- species on a metal site. The CH_3COO^- adsorbs as bidentate chelating, in which both oxygen atoms interact to the same metal atom site, or as bridging, in which the oxygen atoms bind to different metal atom sites. For all surfaces shown in Figure 3, the most stable adsorption structures show

Table 1. The strongest adsorption energies of CH_3COOH, CH_3NH_2, and H_2O on θ-Al_2O_3(110), TiO_2(101), and Nb_2O_5(100) surfaces (in eV).[a]

Adsorbate	θ-Al_2O_3(110)		TiO_2(101)[c]		Nb_2O_5(100)	
	AlO_3	AlO_4	TiO_5-1	TiO_5-2	NbO_5	NbO_6
CH_3COOH	−3.93[b]	−1.21	−1.23	−0.98	−0.83	−0.66
CH_3NH_2	−2.40	−1.85	−1.49	–	−1.14	−1.09
H_2O	−1.92	−1.56	−0.87	–	−0.64	−0.55

[a] The corresponding structures are shown in Figures 3, 4, and S5, for CH_3COOH, CH_3NH_2, and H_2O, respectively. [b] Dissociative adsorption. [c] The stable adsorption of CH_3COOH at TiO_6 site was not found.

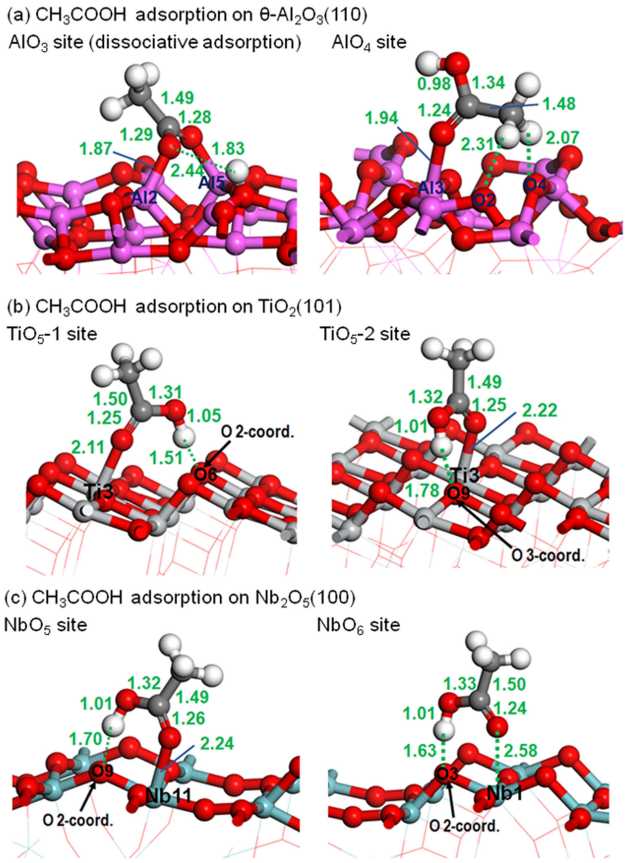

Figure 3. Configurations of (a) CH_3COOH adsorption on θ-Al_2O_3(110) surface at AlO_3 (left) and AlO_4 (right) sites, (b) on TiO_2(101) surface at TiO_5 site with hydrogen bond formed with O 2 atomic coordination number (left) and O 3 atomic coordination number (right) sites, and (c) on Nb_2O_5(100) surface at NbO_5 (left) and NbO_6 (right) sites.

CH_3COOH interacting with the metal sites through the oxygen atom of the C=O group.

The adsorption of CH_3COOH on the AlO_3 site was found to be dissociative (Figure 3(a), left). Both oxygen atoms of CH_3COO^- bind to the AlO_3 sites (bridging on different rows). However, the O–H dissociative structure is assumed to be too stable for further amidation reaction. We examined other possible adsorption configurations, yet we could not locate the nondissociative adsorption of CH_3COOH on the AlO_3 site. The dissociative adsorptions of CH_3COOH on TiO_2(101) and Nb_2O_5 (100) surfaces were also found but were significantly less stable than the nondissociative adsorptions reported in Table 1 by 0.81 and 0.47 eV, respectively.

The adsorption structures of CH_3COOH on TiO_2(101) and Nb_2O_5(100) surfaces include hydrogen bond formation between a hydrogen atom of the carboxylic OH group and an oxygen of the metal oxide surface, in which the bond distances are in the range 1.51–1.78 Å (Figure 3b and 3c). The structure of θ-Al_2O_3 (110) at the AlO_4 site shows that the CH_3 group, instead of the carboxylic OH group, forms very weak hydrogen bonds (bond lengths are 2.07 and 2.31 Å) with the oxygen of the Al_2O_3 surface (Figure 3(a), right).

The adsorption energy trend indicates the weakest adsorption of CH_3COOH on the Nb_2O_5 surface and the strongest adsorption on the Al_2O_3 surface (Table 1). The metal–O(carbonyl) ($M–O_{C=O}$) bond length trend correlates well with the adsorption energy trend. The $M–O_{C=O}$ bond length is in the order Al_2O_3 (1.94 Å) < TiO_2 (2.11 Å) < Nb_2O_5 (2.24 Å). However, a different trend was found in the C=O bond length. Upon adsorption, the carboxylic C=O bond length increases in the order Al_2O_3 (1.24 Å) < TiO_2 (1.25 Å) < Nb_2O_5 (1.26 Å) (free molecule: 1.22 Å). This suggests that upon carboxylic acid adsorption, the C=O bond is most activated on the Nb_2O_5 surface. The trend of this bond activation was also found in the lowest vibrational frequency of the C=O stretching mode of the adsorbed CH_3COOH on the Nb_2O_5 surface and the highest one on the Al_2O_3 surface. The calculated vibrational frequencies of C=O stretching mode for the most stable adsorbed structure are 1685, 1623, and 1616 cm^{-1} on Al_2O_3(110), TiO_2(101), and Nb_2O_5(100), respectively. The qualitative trend agrees well with the respective experimental values of 1697, 1695, and 1686 cm^{-1}.[4]

The partial charges of the adsorbed CH_3COOH and metal oxide surface are shown in Table 2. Charges of the carbonyl oxygen are more negative upon adsorption on all metal oxide surfaces, with the highest negative charge (−1.34 |e|) on θ-Al_2O_3(110), the least negative charge (−1.15 |e|) on Nb_2O_5(100), and a moderate charge of −1.19 |e| on TiO_2(101). The change in metal atom charge due to CH_3COOH adsorption is very small (0.03–0.07 |e|) on all metal oxide surfaces. Charges of the carbonyl oxygen and metal atom on Nb_2O_5(100) show the smallest changes upon adsorption compared to those on θ-Al_2O_3(110) and TiO_2(101). This clearly indicates that the non-electrostatic or covalent-like interaction is relevant, especially for the $Nb–O_{C=O}$ bond.

Here, we focus on the adsorption energy of carbxylic acid and its activation on three surfaces. The higher activities of Nb_2O_5 have experimentally been validated in our previous works.[4–7] The results of *in situ* FT-IR studies[4] support the activation of C=O bond in the carboxylic acids. The adsorption of reactants is a fundamental step for surface-catalyzed reactions. Various characteristic properties of the adsorbed species such as bond distances, bond orders, vibrational frequencies are also frequently used as descriptors to rationalize and predict the catalytic activities.[33,34] Therefore, the adsorption properties are very informative and lead to understanding activation of reactants and eventually the catalytic activities.

3.1.2. Base Tolerance

Basic molecules such as amines (reagents in the amidation reactions discussed here) generally suppress the activity of Lewis acid catalysts by strong adsorption on the acid sites of the catalysts. Based on earlier experiments carried out on the amidation reaction that we investigate in this paper,[4,5] the adsorption of the other reactant, CH_3NH_2, on the three metal oxide surfaces was now examined here. The calculated adsorption energies of CH_3NH_2 on θ-Al_2O_3(110), TiO_2(101), and Nb_2O_5(100) surfaces are summarized in Table 1 and their adsorption configurations are shown in Figure 4.

Table 2. Bader charge (values given in |e|) analysis of metal sites and CH_3COOH upon adsorption on Al_2O_3(110), TiO_2(101), and Nb_2O_5(100).

θ-Al_2O_3(110)			TiO_2(101)				Nb_2O_5(100)			
	clean surface	AlO_4		clean surface	TiO_5-1	TiO_5-2		clean surface	NbO_5	NbO_6
Al_3[a]	+2.44	+2.47	Ti_3	+2.13	+2.20	+2.19	Nb_{11}	+2.62	+2.66	+2.61
O_2	−1.57	−1.57	O_6	−0.97	−1.07	−0.97	Nb_1	+2.67	+2.67	+2.70
O_4	−1.57	−1.56	O_9	−1.15	−1.13	−1.19	O_9	−1.04	−1.09	−1.04
							O_3	−0.98	−0.99	−1.04
CH_3COOH										
	Isolated	at AlO_4		at TiO_5-1			at TiO_5-2	at NbO_5		at NbO_6
O	−1.16	−1.08		−1.18			−1.15	−1.17		−1.14
$O_{C=O}$	−1.11	−1.34		−1.19			−1.17	−1.15		−1.14
C	−0.10	−0.21		−0.14			−0.11	−0.13		−0.16
$C_{C=O}$	+1.50	+1.47		+1.57			+1.54	+1.50		+1.53
Total	0.00	−0.01		+0.04			+0.04	+0.05		+0.05

[a] The atom numbers correspond to the adsorption geometries shown in Figure 3.

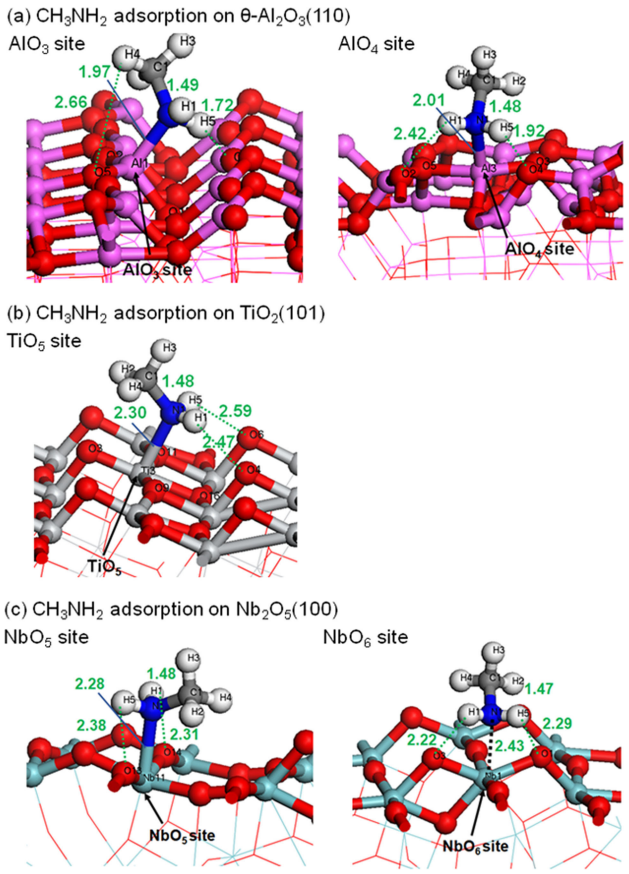

Figure 4. Structures of CH_3NH_2 adsorption on (a) θ-Al_2O_3(110) surface at AlO_3 (left) and AlO_4 (right) sites, (b) TiO_2(101) surface at TiO_5 site, and (c) Nb_2O_5 (100) surface at NbO_5 (left) and NbO_6 (right) sites.

Table 1 shows that the adsorption of CH_3NH_2 is weakest on the Nb_2O_5 surface (−1.16 eV) and strongest on the Al_2O_3 surface (−2.42 eV). The CH_3NH_2 adsorption is non-dissociative on the three surfaces. The atomic coordination environment is responsible for differences in adsorption energy, especially on the Al_2O_3 surface; the adsorption of CH_3NH_2 on the AlO_3 site is considerably stronger than that on the AlO_4 site. The trend in bond distance between the metal and nitrogen atom (M–N) naturally correlates to the trend in adsorption energy, in which the stronger adsorption results in the shorter M–N bond length (Figure 4).

The adsorption of CH_3NH_2 is stronger than that of CH_3COOH on the three surfaces. However, the adsorption of CH_3NH_2 is significantly weak on the Nb_2O_5 surface compared to that on Al_2O_3 and TiO_2 surfaces. This suggests that base poisoning on the Nb_2O_5 surface is less likely to occur compared to Al_2O_3 and TiO_2 surfaces, which allows the metal active sites to be available for the reactant, CH_3COOH, resulting in higher catalytic activity of the Nb_2O_5 catalyst.

The results of Bader charge analysis of CH_3NH_2 adsorption are given in the Supporting Information (Table S3). Upon adsorption on the Nb_2O_5 surface, the partial charge of the N atom varies by only $-0.02|e|$, while it changes by -0.17 and $-0.23|e|$ upon adsorption on the Al_2O_3 and TiO_2 surfaces, respectively. The change in metal charge due to amine adsorption is very small on all surfaces; the change is in the range $+0.00$–$0.04|e|$. This reveals that the interaction between the N atom of the amine and the Nb atom induces very small charge transfer between the N and the NbO_5 site, compared to between N and the AlO_3, AlO_4, and TiO_5 sites, which results in weak adsorption of CH_3NH_2 on the Nb_2O_5 surface.

3.1.3. Water Tolerance

In condensation reactions in which the water molecule is a coproduct, water produced during such reactions can suppress catalytic activity by strong adsorption on acid sites of the catalysts. Substantially weak interaction between water molecules and acidic active sites is required to maintain the high catalytic activity of the catalyst.

Table 1 shows that the calculated H_2O adsorption energy trend is similar to that of CH_3NH_2 adsorption; Nb_2O_5 shows the weakest H_2O adsorption. The Nb_2O_5 catalyst shows the better water tolerance compared to the Al_2O_3 and TiO_2 surfaces. Thus, water, which is a reaction coproduct, is not likely to poison the catalytic active sites, hence leading to the higher catalytic activity on the Nb_2O_5 catalyst. This is in agreement with many previous findings, i.e., that Al_2O_3 is quite reactive toward H_2O. It was found that water molecules dissociate and strongly adsorb on Al_2O_3 and TiO_2 surfaces, with the formation of hydroxylated sites.[35–38] Also, our recent experimental work demonstrated water-tolerant Lewis acid catalysis of the related material, $Nb_2O_5 \cdot nH_2O$.[39] The adsorption geometries of water molecule are shown in Figure S5.

3.2. Metal Oxides: Density of States

Generally, at the Lewis acid site, the charge-transfer or electron-donating interaction occurs between the highest occupied molecular orbital (HOMO) of the adsorbate and the states in the conduction band of the surface. To understand surface–adsorbate interaction in the present system on the three metal oxide surfaces, we analyzed the mean of the partial density of states (PDOS) for the active-site surface atoms referenced to the Fermi level. For example, the mean PDOS of *s*-conduction ($E^*_{s-conduction}$) and *s*-valence ($E^*_{s-valence}$) bands is defined by Equations (2) and (3):[40]

$$E^*_{s-conduction} = \frac{\int_{E_F}^{\infty} \rho_s(\varepsilon)\varepsilon d\varepsilon}{\int_{E_F}^{\infty} \rho_s(\varepsilon) d\varepsilon} \quad (2)$$

$$E^*_{s-valence} = \frac{\int_{-\infty}^{E_F} \rho_s(\varepsilon)\varepsilon d\varepsilon}{\int_{-\infty}^{E_F} \rho_s(\varepsilon) d\varepsilon} \quad (3)$$

where E_F is the Fermi level, $\rho_s(\varepsilon)$is the *s* PDOS, and ε is the energy. By definition, the HOMO of the adsorbate is located at the Fermi level. $E^*_{p-conduction}$, $E^*_{p-valence}$, $E^*_{d-conduction}$, and $E^*_{d-valence}$ were calculated in the same manner, applying the integration over $\rho_p(\varepsilon)$ and $\rho_d(\varepsilon)$. The standard method to align the energy scales of PDOS is applied by shifting the energy scales of PDOS

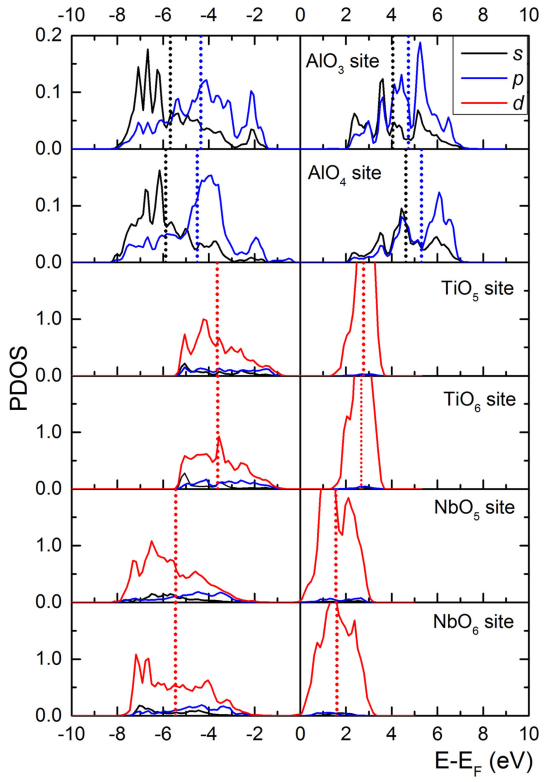

Figure 5. PDOSs of *s*-, *p*-, and *d*-electrons for the AlO_3 and AlO_4 sites of Al_2O_3, Ti surface atom at TiO_5 and TiO_6 sites, and the Nb surface atom at NbO_5 and NbO_6 sites. The vertical dotted lines show the mean PDOSs of *s* (black), *p* (blue), and *d* (red) electrons in the conduction and valence bands. The energy is referenced to the Fermi level and the Fermi level is located at $E - E_F = 0$.

with respect to their Fermi level ($E_F = 0$). The calculated mean PDOS values are tabulated in Tables S5 and S6.

Figure 5 shows the PDOSs of metal surface atoms (possessing different atomic coordination numbers) before adsorption, and the mean PDOSs in the conduction and valence bands (vertical dotted lines). The mean PDOSs of *s*- and *p*-conduction bands of the AlO_3 site are located closer to the Fermi level (closer by ~0.6 eV), than those of the AlO_4 site. Thus, the Al atom at the AlO_3 site tends to accept electrons from the HOMO of the adsorbate more favorably than the Al atom at the AlO_4 site. This suggests that the AlO_3 site could be more active as a Lewis acid than the AlO_4 site, leading to strong interaction at the AlO_3 site, where the spontaneous dissociative adsorption is thermodynamically favorable. Correlation of the mean PDOSs of the *p*-conduction band with the activity of an Al surface atom as Lewis acid has also been reported earlier.[40] Furthermore, the *d* electrons are dominant for the reactivity of metal sites on TiO_2 and Nb_2O_5 surfaces; therefore, we mainly consider *d* electrons for the Ti and Nb sites. However, the descriptor of the mean PDOSs of *d*-conduction bands does not correlate to the adsorption energy difference between TiO_5 and TiO_6 sites and that between NbO_5 and NbO_6 sites (see Figure 5). The NbO_5 and NbO_6 sites show the mean PDOSs of *d*-conduction bands differences of 0.05 eV, while the CH_3COOH adsorption was significantly stronger at the NbO_5 site, by 0.18 eV (Table 1).

Charge transfer upon carboxylic acid adsorption differs between the Al site and the transition metal sites of Ti and Nb atoms. As seen in Table 2, there is a significant charge change upon adsorption of $O_{C=O}$ on the AlO_4 site (0.23 | e |), while adsorptions on the TiO_5 and NbO_5 sites are very small (< 0.08 | e |). This difference is also evident in the change of PDOS at the adsorption site before and after adsorption. Figure 6(a) shows that, upon adsorption, the mean PDOSs of the *s*- and *p*-conduction bands of the AlO_4 site show large energy shifts to higher energies, by 1.1 eV and 0.66 eV, respectively. Therefore, the charge transfer from the HOMO of adsorbates to *s*- and *p*-conduction states of the AlO_4 site (Lewis acid) is seen on the Al_2O_3 surface. However, at the TiO_5, NbO_5, and NbO_6 sites, the $O_{C=O}$ charge change due to adsorption is very small (< 0.08 | e |, Table 2) and the shifts of the mean *d*-conduction states upon adsorption are very small compared with the mean PDOS of the *p*-conduction band of the AlO_4 site; $TiO_5 = 0.09$ eV and $NbO_5 = 0.22$ eV (Figure 6(b and c)). The shifts of the mean PDOSs of the *s*- and *p*-conduction bands of TiO_5 and NbO_5 upon adsorption are also very small (< 0.2 eV) (Figure S6, and Tables S5 and S6). This indicates that the same descriptor (the mean PDOS of the *p*-conduction band) used to probe both the electron acceptance ability as a Lewis acid and adsorbate binding strength of the Al_2O_3 surface could be different from that used to probe that of the TiO_2 and Nb_2O_5 surfaces. It should be noted that the presence of the shifts of the mean *d*-conduction states upon adsorption on the TiO_5 and NbO_5 sites suggests charge transfer from HOMO of adsorbates to the *d*-conduction states on the TiO_2(101) and Nb_2O_5(100) surfaces as well; however, the shifts are much less pronounced than on the Al_2O_3(110) surface.

The interaction between the metal *d*-valence states and the orbitals of adsorbates could be an important factor in understanding the adsorption strength on metal surfaces due to back-donation interaction.[41] The mean PDOS of the *d*-valence band (the *d*-band center theory) of the Ti atom on a clean TiO_2 surface is at higher energy and closer to the Fermi level than that of the Nb atom on a clean Nb_2O_5 surface. Thus, the mean PDOS of the *d*-valence band suggests the stronger adsorption of CH_3COOH on the TiO_2 surface than on the Nb_2O_5 surface.

The plot in the bottom panel of Figure 6 shows the $O_{C=O}(p)$ upon adsorption of CH_3COOH on surfaces. Upon adsorption, the LUMO of $O_{C=O}(p)$ is shifted to the energy level so that it can hybridize with the states in the *d*-conduction bands of the Ti and Nb atoms. Also, the HOMO of $O_{C=O}(p)$ is shifted to the energy level so that it can interact with the states in the *d*-valence bands of the Ti and Nb atoms. Then the onset of the occupied orbitals of $O_{C=O}(p)$ is at approximately the same energy level with the onset of the *d*-valence energy level of the TiO_5 and NbO_5 sites. In contrast, upon adsorption on the Al_2O_3 surface, the LUMO of the O(*p*) carbonyl does not shift to hybridize with most states in the *s*- and *p*-conduction bands of the AlO_4 site. Thus, the PDOSs of $O_{C=O}(p)$ (Figure 6) also provide interesting insight into the difference in the interaction between $O_{C=O}(p)$ with Al(*p*) and between $O_{C=O}(p)$ with Ti(*d*) and Nb(*d*) sites. This indicates that the covalent-like interaction is relevant for the TiO_2 and Nb_2O_5.

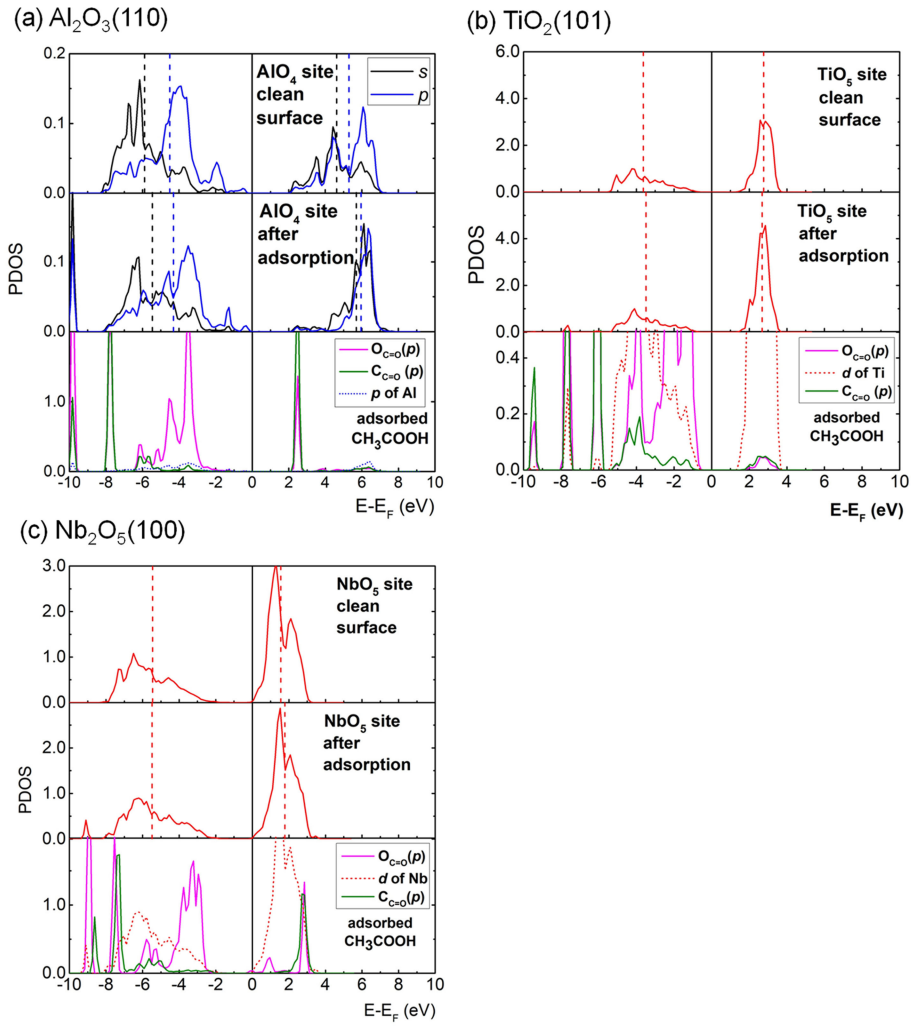

Figure 6. PDOSs of metal active sites before and after CH_3COOH adsorption and PDOSs of $O_{C=O}$ and $C_{C=O}$ of CH_3COOH after adsorption on (a) Al_2O_3(110), (b) TiO_2(101), and (c) Nb_2O_5(100). The top and second panels show PDOSs of *s*, *p*, and *d* electrons of the metal active sites on clean surfaces and after CH_3COOH adsorption, respectively. The bottom panel shows PDOS of *p* electrons of $O_{C=O}$ and $C_{C=O}$ of adsorbed CH_3COOH. The dotted vertical lines show the mean PDOSs of *s*, *p*, and *d* electrons in the conduction and valence bands. The energy is referenced on the Fermi level and the Fermi level is located at $E - E_F = 0$.

For the Al_2O_3 surface, the mean PDOS of the *p*-conduction band of the AlO_4 site and the adsorption energy (E_{ad}) are correlated in the way that the conventional Lewis acid characteristic should possess. The conventional Lewis acid catalyst is anticipated to show the stronger adsorption, with the mean PDOS of the conduction band of the atomic metal located at lower energy, which is closer to its Fermi level. The mean PDOS of the *p*-conduction band of the AlO_3 site located at lower energy and closer to the Fermi energy level clearly identifies the stronger Lewis acidity of the AlO_3 site than that of the AlO_4 site. However, this relationship does not simply hold in the case of the Ti and Nb sites of TiO_2 and Nb_2O_5. The well-known *d*-band center descriptor[41] can apply to the adsorption strength trend at the TiO_5 and NbO_5 sites. The *d*-band center of the TiO_5 site locates closer to the Fermi energy level than that of the NbO_5 site, due to the stronger adsorption on the TiO_5 site.

The Nb_2O_5(100) surface shows the weakest CH_3COOH adsorption, resulting in the longest M-$O_{C=O}$ bond length. However, the adsorbed carboxylic C=O on Nb_2O_5(100) is activated the most, the adsorbed carboxylic C=O bond length increases the most, and the vibrational frequency of the C=O stretching mode is the weakest. The relatively small atomic charge change of $O_{C=O}$ and the hybridization between the PDOS of $O_{C=O}$(*p*) and PDOSs of *d*-conduction bands of Ti and Nb upon adsorption of CH_3COOH indicate that the covalent-like interaction could be relevant to the higher degree of C=O bond activation on the TiO_2 and Nb_2O_5 surfaces than that on the Al_2O_3 surface. Furthermore, analysis suggests that the location of the mean PDOSs of *d*-conduction bands of TiO_2 and Nb_2O_5 and the *p*-conduction band of Al_2O_3 can be correlated to the degree of C=O bond activation: $Nb_2O_5 > TiO_2 > Al_2O_3$.

3.3. Carboxylic Acid Amidation Pathway

The possible reaction mechanism of amidation reaction between carboxylic acid and amine over Nb_2O_5 is shown in Scheme 1.

The produced H^+ and OH^- species on the Nb_2O_5 surface are consumed to form water so that the active sites would not be occupied by these species. The crucial step of amidation reaction is the C–N bond formation between acid and amine (Step 1). Thus, the energy barrier of step (1) were calculated on Al_2O_3(110), TiO_2(101), and Nb_2O_5(100) surfaces and shown in Table 3.

Table 3. Energy barrier (eV) of step (1) C–N bond formation and calculated C=O vibrational frequency ($\nu_{C=O}$, cm^{-1}) of adsorbed carboxylic acid on Al_2O_3 (110), TiO_2(101), and Nb_2O_5(100) surfaces.

Surface	Energy barrier [eV][a]	$\nu_{C=O}$ [cm^{-1}]
Al_2O_3(110)	1.11	1685
TiO_2(101)	0.92	1623
Nb_2O_5(100)	0.84	1616

[a] The corresponding transition state structures are shown in Figure S7.

Nb_2O_5 surface yields the lowest energy barrier of 0.84 eV for C–N bond formation compared to Al_2O_3 and TiO_2 surfaces. The lowest energy barrier of the C–N bond formation on Nb_2O_5 surface could result from that the C=O bond is most activated on Nb_2O_5 showing the C=O longest bond length and the lowest vibration frequency of C=O stretching mode upon adsorption as discussed in section 3.1.1. The trend of C–N bond formation energy barrier, ($Nb_2O_5 < TiO_2 < Al_2O_3$) agrees with the trend of C=O bond activation which is evident by the vibration frequency C=O stretching mode.

4. Conclusions

To understand the performance of the recently developed direct amide bond formation on metal oxide surfaces, we investigated the C=O bond activation of carboxylic acid on Al_2O_3, TiO_2, and Nb_2O_5 surfaces. DFT calculations were performed for the θ-Al_2O_3(110), anatase TiO_2(101), and T-Nb_2O_5 (100) surfaces. The reactive adsorption sites of carboxylic acid were found to be at the AlO_4, TiO_5, and NbO_5 sites. The adsorption energies of carboxylic acid were in the order $Al_2O_3 > TiO_2 > Nb_2O_5$, while the bond activation of C=O and its vibrational frequency showed the opposite trend. This means that the C=O bond activation of the carbonyl group is most efficient on Nb_2O_5(100) surface, although the adsorption energy is larger on the Al_2O_3 and TiO_2 surfaces. The base and water tolerance of the metal oxide surfaces is also a crucial factor for the catalysts of direct amidation reactions. The adsorption of CH_3NH_2 is significantly weak on Nb_2O_5 compared to that on Al_2O_3 and TiO_2 surfaces. Water molecule is also adsorbed substantially weak on Nb_2O_5 surface. These suggest that Nb_2O_5 surface possess better base and water tolerance property than Al_2O_3 and TiO_2 surfaces. Furthermore, the most activation of the C=O bond on Nb_2O_5 leads to the lowest energy barrier of C–N bond formation which is the key step of the amidation. These crucial factors are the origin for the high activity of the Nb_2O_5 surface in the direct amidation reaction.

The relevant covalent-like interaction found in Nb_2O_5, which is seen in the hybridization between the PDOS of the Nb *d*-conduction band and the PDOS of $O_{C=O}$(*p*), accompanied by adsorption of CH_3COOH, indicates the important role it plays in carbonyl C=O bond activation. Therefore, unlike the standard interpretation of the Lewis acid site of metal oxide surfaces, the covalent-like interaction between carbonyl group of carboxylic acid and metal site is shown to be relevant in carbonyl C=O bond activation and, consequently, in the reactivity of the present direct amidation reaction of carboxylic acids and amines. The position of the mean PDOS of the *d*-conduction band demonstrates a good correlation with the degree of carbonyl C=O bond activation; namely, the donative interaction between carbonyl HOMO and metal unoccupied *d*-orbital. The closer the mean PDOS of the *d*-conduction band to the Fermi level, the higher the degree of carbonyl C=O bond activation on the Lewis acid site of the metal oxide. This new understanding of the Lewis acid site elucidates the reason for Nb_2O_5 being the most effective heterogeneous catalyst for the direct amidation of carboxylic acids among the metal oxide surfaces examined here. Furthermore, it is useful for the further development of heterogeneous catalysts.

Associated Content

Supporting Information

Bulk structures, XRD patterns of the Nb_2O_5 catalyst, Charge density differences, H_2O adsorption structures, Bader charges with the adsorption of CH_3NH_2 and H_2O, and Transition state structures.

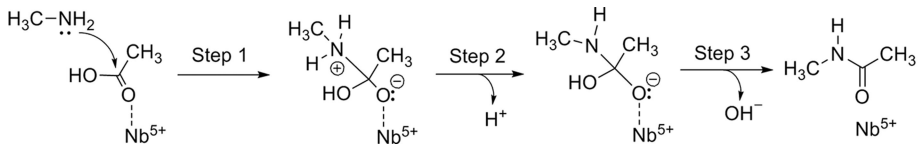

Scheme 1. Possible reaction mechanism of amidation reaction between carboxylic acid and amine over Nb_2O_5.

Acknowledgments

This work was supported by a MEXT program (Ministry of Education Culture, Sports, Science and Technology in Japan) "Elements Strategy Initiative to Form Core Research Center." M. E. acknowledges the financial support from a Grant-in-Aid for Scientific Research, Japan Society for the Promotion of Science (JSPS), JP16H04104 and JP16H06511. This work was also supported by the CREST program (Japan Science and Technology Agency), JPMJCR17J3. The computations were partially performed at the Research Center for Computational Science, Okazaki, Japan.

Conflict of Interest

The authors declare no conflict of interest.

Keywords: Nb_2O_5 · amidation · carboxylic acids · C=O bond activation · density functional calculations · Lewis acid catalysis

[1] D. J. C. Constable, P. J. Dunn, J. D. Hayler, G. R. Humphrey, J. J. L. Leazer, R. J. Linderman, K. Lorenz, J. Manley, B. A. Pearlman, A. Wells, A. Zaks, T. Y. Zhang, *Green Chem.* **2007**, *9*, 411–420.
[2] H. Lundberg, F. Tinnis, N. Selander, H. Adolfsson, *Chem. Soc. Rev.* **2014**, *43*, 2714–2742.
[3] K. Nakajima, Y. Baba, R. Noma, M. Kitano, J. N. Kondo, S. Hayashi, M. Hara, *J. Am. Chem. Soc.* **2011**, *133*, 4224–4227.
[4] M. A. Ali, S. M. A. H. Siddiki, W. Onodera, K. Kon, K. Shimizu, *ChemCatChem* **2015**, *7*, 3555–3561.
[5] M. A. Ali, S. M. A. H. Siddiki, K. Kon, K. Shimizu, *ChemCatChem* **2015**, *7*, 2705–2710.
[6] M. A. Ali, S. M. A. H. Siddiki, K. Kon, J. Hasegawa, K. Shimizu, *Chem. Eur. J.* **2014**, *20*, 14256–14260.
[7] M. A. Ali, S. K. Moromi, A. S. Touchy, K. Shimizu, *ChemCatChem* **2016**, *8*, 891–894.
[8] S. Kobayashi, K. Manabe, *Acc. Chem. Res.* **2002**, *35*, 209–217.
[9] Y. Koito, K. Nakajima, H. Kobayashi, R. Hasegawa, M. Kitano, M. Hara, *Chem. Eur. J.* **2014**, *20*, 8068–8075.
[10] J. P. Perdew, K. Burke, M. Ernzerhof, *Phys. Rev. Lett.* **1996**, *77*, 3865–3868.
[11] J. P. Perdew, K. Burke, M. Ernzerhof, *Phys. Rev. Lett.* **1997**, *78*, 1396–1396.
[12] G. Yamaguchi, I. Yasui, W.-C. Chiu, *Bull. Chem. Soc. Jpn.* **1970**, *43*, 2487–2491.
[13] C. Wolverton, K. C. Hass, *Phys. Rev. B* **2000**, *63*, 024102.
[14] K. Kato, S. Tamura, *Acta Crystallogr. B* **1975**, *31*, 673–677.
[15] P. E. Blöchl, *Phys. Rev. B* **1994**, *50*, 17953–17979.
[16] G. Kresse, D. Joubert, *Phys. Rev. B* **1999**, *59*, 1758–1775.
[17] J. K. Burdett, T. Hughbanks, G. J. Miller, J. W. Richardson, J. V. Smith, *J. Am. Chem. Soc.* **1987**, *109*, 3639–3646.
[18] P. Hirunsit, K. Shimizu, R. Fukuda, S. Namuangruk, Y. Morikawa, M. Ehara, *J. Phys. Chem. C* **2014**, *118*, 7996–8006.
[19] Z. Lodziana, N. Y. Topsoe, J. K. Nørskov, *Nat. Mater.* **2004**, *3*, 289–293.
[20] Y. Sakashita, Y. Araki, H. Shimada, *Appl. Catal. A* **2001**, *215*, 101–110.
[21] P. Nortier, P. Fourre, A. B. M. Saad, O. Saur, J. C. Lavalley, *Appl. Catal.* **1990**, *61*, 141–160.
[22] G. S. Foo, D. Wei, D. S. Sholl, C. Sievers, *ACS Catal.* **2014**, *4*, 3180–3192.
[23] G. Kresse, J. Furthmüller, *Phys. Rev. B* **1996**, *54*, 11169–11186.
[24] G. Kresse, J. Furthmüller, *Comput. Mater. Sci.* **1996**, *6*, 15–50.
[25] S. Grimme, *J. Comput. Chem.* **2006**, *27*, 1787–1799.
[26] S. Grimme, J. Antony, S. Ehrlich, H. Krieg, *J. Chem. Phys.* **2010**, *132*, 154104.
[27] C. L. Fu, K. M. Ho, *Phys. Rev. B* **1983**, *28*, 5480–5486.
[28] G. Henkelman, A. Arnaldsson, H. Jónsson, *Comput. Mater. Sci.* **2006**, *36*, 354–360.
[29] E. Sanville, S. D. Kenny, R. Smith, G. Henkelman, *J. Comput. Chem.* **2007**, *28*, 899–908.
[30] W. Tang, E. Sanville, G. Henkelman, *J. Phys. Condens. Matter* **2009**, *21*, 084204.
[31] G. Henkelman, H. Jónsson, *J. Chem. Phys.* **2000**, *113*, 9978–9985.
[32] G. Henkelman, H. Jónsson, *J. Chem. Phys.* **1999**, *111*, 7010–7022.
[33] W. E. Farneth, R. J. Gorte, *Chem. Rev.* **1995**, *95*, 615–635.
[34] C. Liu, I. Tranca, R. A. V. Santen, E. J. M. Hensen, E. A. Pidko, *J. Phys. Chem. C* **2017**, *121*, 23520–23530.
[35] J. Blomquist, L. E. Walle, P. Uvdal, A. Borg, A. Sandell, *J. Phys. Chem. C* **2008**, *112*, 16616–16621.
[36] Z. Zhao, Z. Li, Z. Zou, *J. Phys. Chem. C* **2012**, *116*, 7430–7441.
[37] M. Digne, P. Sautet, P. Raybaud, P. Euzen, H. Toulhoat, *J. Catal.* **2004**, *226*, 54–68.
[38] M. Digne, P. Sautet, P. Raybaud, H. Toulhoat, E. Artacho, *J. Phys. Chem. B* **2002**, *106*, 5155–5162.
[39] M. N. Rashed, S. M. A. H. Siddiki, M. A. Ali, S. K. Moromi, A. S. Touchy, K. Kon, T. Toyao, K. Shimizu, *Green Chem.* **2017**, *19*, 3238–3242.
[40] G. R. Jenness, M. A. Christiansen, S. Caratzoulas, D. G. Vlachos, R. J. Gorte, *J. Phys. Chem. C* **2014**, *118*, 12899–12907.
[41] B. Hammer, J. K. Nørskov, *Surf. Sci.* **1995**, *343*, 211–220.

Manuscript received: July 28, 2018
Accepted Article published: August 15, 2018
Version of record online: September 3, 2018